

Trans-dimensional gravity and magnetic joint inversion for 3-D earth models

Emad Ghalenoei¹, Jan Dettmer,² Mohammed Y. Ali³ and Jeong Woo Kim¹

¹Department of Geomatics Engineering, University of Calgary, 2500 University Dr NW, Calgary, AB T2N 1N4, Canada. E-mail:
emad.ghalenoei@ucalgary.ca

²Department of Geoscience, University of Calgary, 2500 University Dr NW, Calgary, AB T2N 1N4, Canada

³Department of Earth Sciences, Khalifa University of Science and Technology, P.O. Box 127788, Abu Dhabi, UAE

Accepted 2022 February 23. Received 2022 February 22; in original form 2021 October 11

SUMMARY

Studying 3-D subsurface structure based on spatial data is an important application for geophysical inversions. However, major limitations exist for conventional regularized inversion when applied to potential-field data. For example, global regularization parameters can mask model features that may be important for interpretation. In addition, 3-D inversions are typically based on data acquired in 2-D at the Earth's surface. Such data may contain significant spatial error correlations in 2-D due to the choice of spatial sampling, acquisition geometry, ambient noise and model assumptions. These correlations can cause trade-offs with spatial resolution and should be accounted for. However, correlations are often ignored, particularly 2-D correlations in spatial data, such as potential field data recorded on the Earth's surface. Non-linear Bayesian methods can address these shortcomings and we present a new hierarchical model for 2-D correlated errors. Nonetheless, limitations also exist. For example, non-linear Bayesian estimation requires numerical integration with a considerable computational burden to collect a posterior ensemble of models. For 3-D applications, this cost can be prohibitive. This paper presents a non-linear Bayesian inversion with trans-dimensional (trans-D) partitioning of space by a hierarchy of Voronoi nodes and planes (VP), and trans-D estimation of the data noise covariance matrix. The addition of planes permits the introduction of prior information which reduces non-uniqueness. The covariance matrix estimation uses a trans-D autoregressive (AR) noise model to quantify correlated noise on 2-D potential-field data. We address computational cost by wavelet compression in the forward problem and by basing susceptibility on an empirical relationship with density contrast. The method is applied to simulated data and field data from off-shore Abu Dhabi. With simulated data, we demonstrate that subsurface structures are well-resolved with the trans-D model that applies hierarchical VP partitioning. In addition, the model locally adapts based on data information without requiring regularization. The method is also successful in reducing 2-D error correlation via trans-D AR models in 2-D. From field data, the inversion efficiently resolves basement topography and two distinct salt diapirs with a parsimonious and data-driven parametrization. Results show a considerable reduction in 2-D spatial correlations of field data using the proposed trans-D AR model.

Key words: Gravity anomalies and Earth structure; Magnetic anomalies: modelling and interpretation; Inverse theory; Joint inversion; Probability distributions; Statistical methods.

1 INTRODUCTION

Inversion of gravity and magnetic anomalies is widely used to map density and susceptibility structure in the Earth's subsurface (Blakely 1996). The density and susceptibility anomalies are often used to identify subsurface structures and targets appropriate for further studies in applications such as mining exploration (Martinez *et al.* 2010; Kamm *et al.* 2015), crustal structure (Aitken *et al.* 2013) and hydrocarbon exploration (Jorgensen & Kisabeth 2000; Krahenbuhl & Li 2009; Silva Dias *et al.* 2011; Geng *et al.* 2020; Ghalenoei *et al.* 2021). In common 3-D potential field inversions, model space is parametrized by regular 3-D prisms (Li & Oldenburg 1996; Boulanger & Chouteau 2001; Silva Dias *et al.* 2011; Uieda & Barbosa 2012; Martinez *et al.* 2013) that overparametrize the problem. Therefore, regularization is required to

solve the inverse problem (Li & Oldenburg 1998; Pallero *et al.* 2017; Uieda & Barbosa 2017; Maag & Li 2018). As a result, the solution and its uncertainty can reflect the constraints of the chosen regularization (Hawkins & Sambridge 2015). In such cases, the model spatial resolution is uniform while data spatial resolution is likely irregular. Therefore, irregular meshes provide advantages for model partitioning, but these may be difficult to be solved via linearization due to computationally intensive forward calculation, numerical instabilities of partial derivatives, near-singular values in the kernel matrix (Michelini 1995) and dependency on initial models. Various types of irregular meshes have been proposed for geophysical inversions, including tetrahedral 3-D meshes (Sambridge *et al.* 1995; Stenerud *et al.* 2009; Lelievre & Farquharson 2013), adaptive-grids (Michelini 1995), deformable-layer and cell tomography (Zhou *et al.* 2010) and Voronoi cells (Bodin *et al.* 2009). Notably, irregular meshes can significantly reduce the dimensionality of the model but may still require regularization.

Depending on geometry and density contrast assumptions, two types of inverse problem are commonly considered. The first type assumes known geometry but unknown density contrast or magnetic susceptibility (Li & Oldenburg 1998; Portniaguine & Zhdanov 2002; Lelievre *et al.* 2019). The second type assumes known density contrast but unknown geometries. The latter is commonly solved by non-linear optimization (Camacho *et al.* 2000; Krahnenbuhl & Li 2009; Uieda & Barbosa 2012). All these methods incur high computational cost for large kernel matrix and model vector multiplications. To reduce cost, some works suggested the fast Fourier transform for this multiplication (Wu 2016; Chen & Liu 2019). However, this approach requires data coverage to lie exactly above the model space, hence this is not generally applicable to gravity and magnetic inversions where model space is extended beyond data coverage to minimize edge effects. Alternatively, 3-D wavelet compression has achieved substantial gains in computational efficiency (Li & Oldenburg 2003).

To overcome regularization requirements, trans-dimensional (trans-D) sampling (Green 1995) has been applied in geophysics (Sambridge *et al.* 2006). In trans-D models, the number of parameters varies during sampling. Thereby, the method locally adapts the parametrization based on data information (Malinverno & Leaney 2000; Bodin & Sambridge 2009). To date, many geophysical inversions have successfully applied trans-D models (Bodin & Sambridge 2009; Dettmer & Dosso 2012; Kolb & Lekić 2014; Piana Agostinetti *et al.* 2015; Pilia *et al.* 2020; Ray 2021), including some applications to potential field data (Luo 2010; Izquierdo *et al.* 2020; Ghalenoei *et al.* 2021).

Appropriate treatment of data noise is important for geophysical inference. In particular, when correlated errors may be present (Dettmer *et al.* 2007), but noise is typically not known independently. To capture the effect of unknown, correlated noise on parameter uncertainties, a parametric noise model can be included in the inversion (Dettmer *et al.* 2012; Kolb & Lekić 2014). Parametric noise models can include scale and correlation parameters as unknowns in hierarchical Bayesian approaches. However, most previous studies are limited to correlations in 1-D.

We present a new parametrization method that applies trans-D spatial and trans-D AR noise models to a 3-D non-linear joint gravity and magnetic Bayesian inversion. The spatial partitioning is constructed with a hierarchy of 3-D Voronoi cells and six planes (VP). Augmenting the Voronoi cells with six planes permits the introduction of additional prior constraints that reduce non-uniqueness. In particular, the planes are used to assign rock types to groups of Voronoi nodes (Ghale noe *et al.* 2021). Planes are chosen over other possible partitioning hierarchies since the computational cost associated with partitioning by planes is small. Computational cost is also reduced by applying a wavelet transform to reduce the cost in evaluating the forward problem (Li & Oldenburg 2003).

The trans-D noise model is implemented by a 2-D autoregressive (AR) model with unknown AR orders for both gravity and magnetic data. The model can capture spatial correlation in the 2-D data acquisition plane. The correlations are described by two AR models for the horizontal directions and a third AR model for the diagonal direction.

The method is applied to simulated and field aerogravity and aeromagnetic data. Results for simulated data show benefits of trans-D AR models in 2-D combined with the VP partitioning. It demonstrates that various geometries of model features can be imaged. In addition, the true noise model is reasonably resolved using the proposed AR model. The field data are from offshore Abu Dhabi, United Arab Emirates (UAE), where complex salt tectonics are known to exist (Ali *et al.* 2017; Geng *et al.* 2020). The trans-D noise model is particularly suitable for these data since the high spatial sampling rates in aerial acquisition can lead to strongly correlated errors. Our model from the field data will be compared with a previous work that used a linearized inversion method and seismic profiles. The application demonstrates successful decorrelation of data residuals, infers multiple salt structures in the presence of basement topography and produces excellent data fits.

2 METHODS

2.1 Bayesian approach and trans-dimensional sampling

This section briefly reviews the Bayesian framework in inverse problems (Mosegaard & Tarantola 1995; Sambridge & Mosegaard 2002; MacKay *et al.* 2003) and the trans-D method used in this study. For a more complete treatment, we recommend other works (e.g. Green 1995; Sambridge *et al.* 2006). Let $\mathbf{d} \in \mathbb{R}^N$ be a random variable of N observed data. In addition, let $\mathbf{m}_k \in \mathcal{M}_k$ denote a vector of random variables. Importantly, \mathbf{m}_k contains a choice of parametrization for spatial partitioning and data residuals noise, and various assumptions about the physics of the earth model. Bayes' theorem (Green 1995) for a trans-D model ($\mathbf{m}_k | k$) can be written

$$P(\mathbf{m}_k, k | \mathbf{d}) = \frac{P(\mathbf{d} | \mathbf{m}_k, k)P(\mathbf{m}_k | k)P(k)}{\sum_{k' \in K} \int_{\mathcal{M}} P(\mathbf{d} | \mathbf{m}'_{k'}, k')P(\mathbf{m}'_{k'} | k')P(k')d\mathbf{m}'_{k'}}, \quad (1)$$

where K is a countable set of model choices, $k \in K$ is the index of possible choices of models, $P(k)$ is the prior probability distribution function (pdf) for k , integration is over the state space \mathcal{M} , $P(\mathbf{m}_k | k)$ is the prior for \mathbf{m}_k given k , $P(\mathbf{d} | \mathbf{m}_k, k)$ is the likelihood function, hereafter represented by $\mathcal{L}(\mathbf{m}_k, k)$ and $P(\mathbf{m}_k, k | \mathbf{d})$ is the posterior pdf of model parameters that represents the solution of the inversion. The posterior pdf can be estimated by numerical integration. For example, Green (1995) uses the Metropolis–Hastings–Green (MHG) algorithm, where a proposed model $\mathbf{m}'_{k'}$ is generated by a proposal pdf $Q(\mathbf{m}'_{k'} | \mathbf{m}_k)$, and jumps between the various models indexed by k are permitted. Here, three steps including *add*, *delete* and *perturb* are applied in the trans-D sampling. The *add* and *delete* steps allow changing the number of model parameters. The *perturb* step keeps the model dimensionality and perturbs a parameter chosen uniformly random by a focused proposal distribution.

In this study, two types of proposal distributions are applied. For steps that do not change dimension, a focused Cauchy proposal is applied, where the scaling parameter is tuned based on acceptance rates. Since the Cauchy proposal is symmetric and the prior is uniform, the acceptance probability simplifies to the likelihood ratio. For *add* and *delete* steps, the prior distribution is used as the proposal. Due to the penalty involved in the MHG acceptance for focused proposals, proposing from the prior has been shown to be more computationally efficient (Dosso *et al.* 2014). As a result, the Jacobian appearing in the MHG acceptance is unity, and prior and proposal ratios cancel. Therefore, all acceptance probabilities in this work only require the computation of likelihood ratios, even though two different proposal distributions are applied.

2.2 Noise parametrization with 2-D spatial covariance estimation

We propose a noise model to address correlated data errors for spatial observations taken at the Earth's surface. The likelihood function $\mathcal{L}(\mathbf{m}_k)$ includes assumptions about data-error statistics and Gaussian noise assumptions are common, resulting in

$$\log \mathcal{L}(\mathbf{m}_k) = -\frac{N}{2} \log_e(2\pi) - \frac{1}{2} \log_e(|\mathbf{C}_r|) - \frac{1}{2} \mathbf{r}^\top \mathbf{C}_r^{-1} \mathbf{r}, \quad (2)$$

where N is the number of data, $\mathbf{r} = \mathbf{d}^{obs} - \mathbf{d}(\mathbf{m}_k)$ are the data residuals and \mathbf{C}_r is the data residuals covariance matrix. For 2-D data, \mathbf{C}_r includes spatial correlations in the horizontal directions. Note that these correlations can be described by dependence on the two horizontal directions and a diagonal direction. We introduce a trans-D AR model for 2-D data residuals with the AR orders (p) estimated by data. As a result, posterior inferences include uncertainty due to the limited knowledge available for choosing the AR orders. The logarithm of the likelihood function for applying a trans-D AR model for 2-D is unchanged from the 1-D case (Dettmer *et al.* 2012)

$$\log \mathcal{L}(\mathbf{m}_k) = -\frac{N}{2} \log_e(2\pi) - N \log_e(\sigma) - \frac{1}{2} \left(\frac{\mathbf{d}^{obs} - \mathbf{d}(\mathbf{m}_k) - \lambda(\mathbf{m}_p^{AR})}{\sigma} \right)^\top \left(\frac{\mathbf{d}^{obs} - \mathbf{d}(\mathbf{m}_k) - \lambda(\mathbf{m}_p^{AR})}{\sigma} \right), \quad (3)$$

where σ is an unknown standard deviation that can be implicitly computed by $\sigma = \sqrt{\frac{\|\mathbf{r}\|^2}{N}}$, where $\|\cdot\|$ is the L2 norm. The term $\lambda(\mathbf{m}_p^{AR})$ are 2-D data residuals predicted by the AR process with order p and $\frac{\mathbf{d}^{obs} - \mathbf{d}(\mathbf{m}_k) - \lambda(\mathbf{m}_p^{AR})}{\sigma}$ are residuals assumed to be uncorrelated due to application of the AR prediction, and standardized due to scaling by σ . The AR process produces 2-D correlations in the two horizontal (x and y) and diagonal (xy) directions. Hence, \mathbf{m}_p^{AR} is decomposed into the three trans-D AR models \mathbf{AR}_x , \mathbf{AR}_y and \mathbf{AR}_{xy} . Each model is for one spatial dimension with $\mathbf{AR}_x = [\varphi_1^x, \varphi_2^x, \dots, \varphi_{p_x}^x]$, $\mathbf{AR}_y = [\varphi_1^y, \varphi_2^y, \dots, \varphi_{p_y}^y]$ and $\mathbf{AR}_{xy} = [\varphi_1^{xy}, \varphi_2^{xy}, \dots, \varphi_{p_{xy}}^{xy}]$, where φ_j^t are AR coefficients. To implement this trans-D AR process for data residuals stored in a 2-D array, we insert the AR coefficients as

$$\mathbf{m}_p^{AR} = \begin{bmatrix} 0 & \varphi_1^x & \varphi_1^x & \dots & \varphi_{p_x}^x \\ \varphi_1^y & \varphi_1^{xy} & 0 & 0 & 0 \\ \varphi_2^x & 0 & \varphi_2^{xy} & 0 & 0 \\ \vdots & 0 & 0 & \ddots & 0 \\ \varphi_{p_y}^y & 0 & 0 & 0 & \varphi_{p_{xy}}^{xy} \end{bmatrix}. \quad (4)$$

We assume the maximum orders for p_x , p_y and p_{xy} to be 3. Therefore, each \mathbf{AR}_x , \mathbf{AR}_y or \mathbf{AR}_{xy} can have up to three coefficients. In cases where \mathbf{AR}_x , \mathbf{AR}_y and \mathbf{AR}_{xy} have less than 3 coefficients (since the models are trans-D), zero is inserted for missing coefficients. Note that inserted zeros will not be considered as parameters. As a result, \mathbf{m}_p^{AR} would be a square matrix of size 4 by 4.

To apply this AR model in the inversion, it is included in the MHG sampling. For MHG updates, a direction is randomly chosen (x , y or xy), then an MHG step is randomly chosen (*add*, *delete* or *perturb*) and applied to the appropriate AR coefficients. Note that an AR(0) model, \mathbf{m}_0^{AR} , has no coefficient and represents uncorrelated residuals. In this case, MHG only permits an *add* step, which is sampled from the prior pdf. When the AR model reaches maximum order, no *add* step is possible and the probabilities of *add*, *delete* and *perturb* are 0, 1/3 and 2/3, respectively. In all other cases, MHG steps have an equal probability of 1/3. Finally, $\lambda(\mathbf{m}_p^{AR})$ for a proposed model is computed by

$$\lambda(\mathbf{m}_p^{AR})(t_x, t_y) = \sum_{i=0}^3 \sum_{j=0}^3 m_p^{AR}(i, j) r(t_x - i, t_y - j) + \epsilon(t_x, t_y), \quad (5)$$

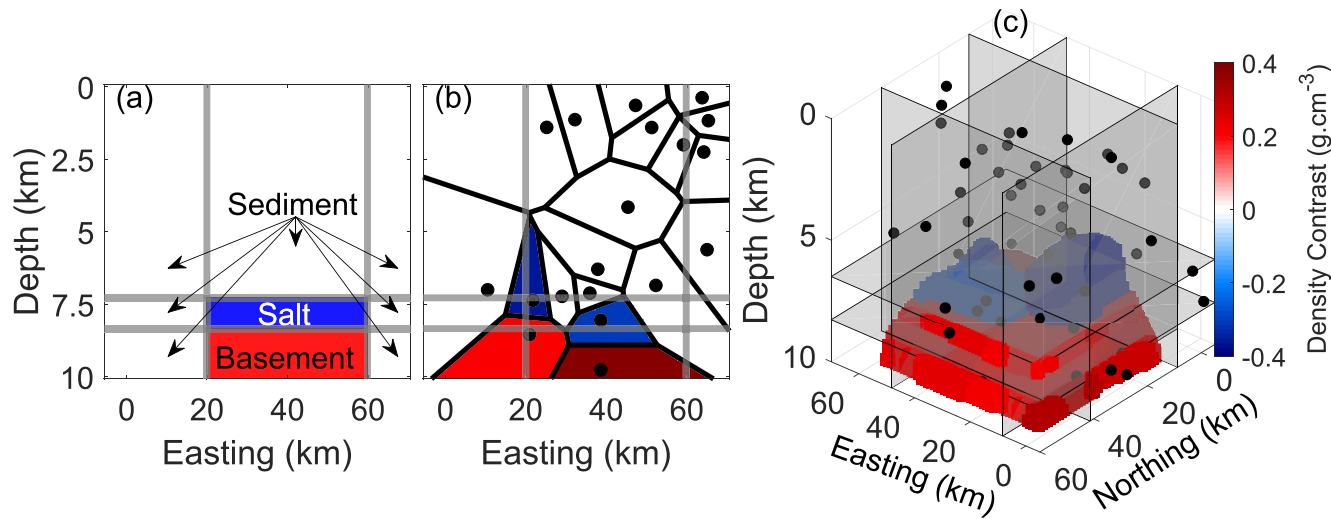


Figure 1. An example of the VP parametrization for 2-D space. (a) Nine subspaces resulting from two horizontal and two vertical grey lines. (b) The Voronoi diagram is shown with black lines and nodes. (c) The VP parametrization for 3-D space where six planes and Voronoi nodes are shown by grey planes and black dots, respectively.

where t_x and t_y index the 2-D-array data, ϵ is a 2-D array of uncorrelated Gaussian noise, and i and j index the matrix elements in eq. (4). To maintain the stationarity of the AR prediction, we define individual uniform bounded priors for the coefficients at each order. This is achieved by a preliminary test to show the appropriate prior bounds satisfy the stationarity. The stationary condition can be represented in terms of a polynomial lag with roots outside the unit circle (Mojiri *et al.* 2018). In addition, stationary AR models require lower orders to be present before higher orders are introduced. Therefore, we apply *add* and *delete* steps for AR coefficients only at the end of the current AR model vector.

2.3 Hierarchical spatial partitioning with Voronoi cells and planes

Data predictions in this method are based on a grid of regular prisms, where the discretization is chosen to be smaller than the spatial resolution power of the data. To this grid, we apply 3-D Voronoi partitioning by k Voronoi nodes. The MHG sampling considers a range of k values and can *jump* between models indexed by the various k . For application to potential field data, the success of this approach depends on how physical properties (density contrast or susceptibility) are assigned to Voronoi cells. If little prior knowledge is applied, significant non-uniqueness can cause implausible depths and locations of rock formations. Previous works applied nested Voronoi partitioning and alpha shapes to improve the imaging of rock formations in 2-D (Ghale noe *et al.* 2021; Ghale noe 2022). However, nested Voronoi partitioning exhibited signs of underparametrization when compared to alpha shapes. In addition, alpha shapes add computational burden which is currently not feasible in 3-D. Therefore, we propose a computationally efficient approach based on a hierarchy of Voronoi nodes and vertical and horizontal planes (VP) to consider the high-dimensional models for 3-D structures.

Fig. 1 illustrates the VP parametrization schematically with 2-D and 3-D examples. In Fig. 1(a), the locations of the two horizontal grey lines and the two vertical grey lines are inversion parameters. The locations of these four lines partition the 2-D space into nine subspaces. A rock type can be assigned to each subspace to introduce prior geological constraints. In this example, we assign rock salt to the central subspace, basement rocks to the bottom-centre subspace and sedimentary rocks to the remaining subspaces (Fig. 1a). The Voronoi cells are then combined with the lines as an additional hierarchy of partitioning (Fig. 1b). Locations of Voronoi nodes are independent of the locations of the four lines. However, depending on which subspace a Voronoi node is in, a rock type will be assigned to the Voronoi node. For example, Fig. 1(b) shows that two Voronoi nodes are assigned a rock salt density contrast. This approach assumes that rock formations are mostly continuous and avoids fragmentation. Note that even though the four lines introduce regular partitioning, the Voronoi diagram introduces irregular partitioning. This results in mostly continuous rock masses but significant freedom with respect to shape. For example, rock salt in Fig. 1(b) protrudes sharply.

The 2-D approach is extended to 3-D by using six planes (two horizontal and four vertical) instead of 4 lines and 3-D Voronoi cells instead of 2-D Voronoi cells. The six planes are defined by six inversion parameters (X_1, X_2, Y_1, Y_2, Z_1 and Z_2) and geological constraints are the three rock types (sedimentary rocks, rock salt and basement rocks). Each plane is perpendicular to an axis in 3-D Cartesian coordinates. Therefore, the k Voronoi nodes are divided into 27 subspaces by the six planes (Fig. 1c). The main advantages of this approach are high computational efficiency and few parameters compared to nested Voronoi partitioning. The main disadvantage of the approach is that rock types must be assigned to the 27 subspaces which require consideration of geological information and some experience. The prior distributions

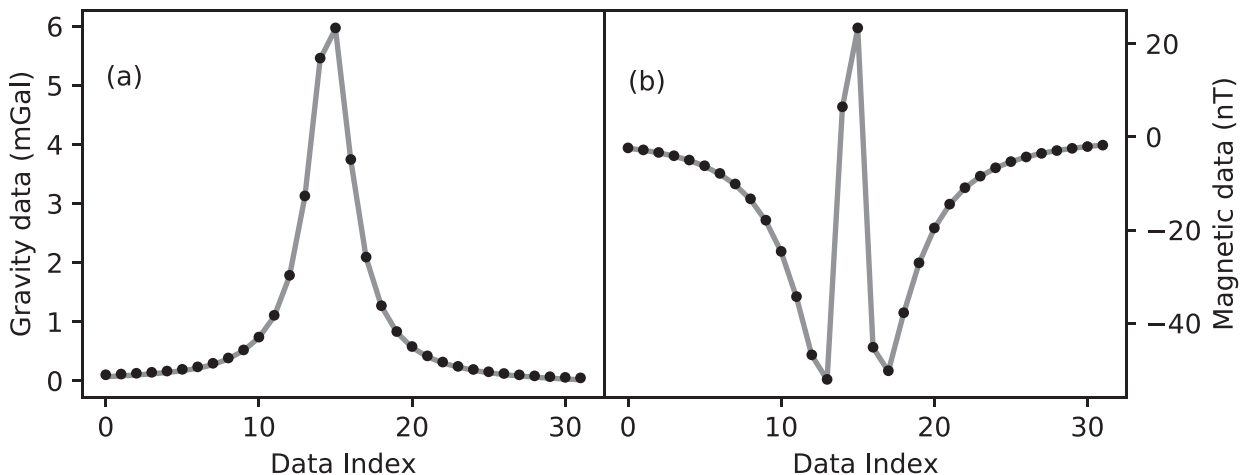


Figure 2. (a) A slice through gravity data computed from a sparse matrix based on wavelet compression (grey line) and true gravity data (black dots). (b) The same information for magnetic data.

for the six plane parameters and Voronoi node locations [x , y , z] are bounded and uniform. The prior for density contrast is uniform over $(\Delta\rho^{\min}, \Delta\rho^{\max})$, and the minimum and maximum bounds are distinct for rock types.

To limit parametrization complexity, basement susceptibilities are computed from density contrasts assuming an empirical ratio of $\frac{\Delta\rho}{\chi}$ (Li & Oldenburg 1998). Sedimentary rocks and rock salt are assumed to have zero susceptibility. Therefore, density contrast and susceptibility models share the same structural boundaries in the joint inversion.

In gravity and magnetic inversions, it is recommended that the horizontal axes extent should be approximately five times greater than the depth of targets of interest (Hinze *et al.* 2013). Such extents cause Voronoi diagrams to be aligned in the direction of the shorter axis (depth), leading to poor partitioning for our purposes. To avoid this issue, we normalize axes to unity for the purpose of the Voronoi partitioning.

2.4 Efficient forward model and sampling

For computational efficiency, the 3-D Voronoi cells are mapped to fixed regular prisms by the nearest neighbours (NN) algorithm (Fix & Hodges 1989; Altman 1992). We use the open-source *faiss* library (Johnson *et al.* 2019) for an efficient NN search. In addition, the underlying regular grid permits straightforward data predictions. The gravity forward model for M regular prisms of density contrast $\Delta\rho$ is carried out by summing over the product of gravity kernel and density contrast (e.g. see eq. 9.3 in Blakely 1996). In the same manner, magnetic anomalies are predicted from susceptibility values and the magnetic kernel (e.g. see eq. 9.19 in Blakely 1996). Since the regular grid does not change, the kernel matrices are computed only once and saved for the inversion.

Although precomputed kernel matrices gain efficiency, large kernel matrices still cause a substantial memory and computational time burden. To overcome these issues, the matrix–vector multiplication can be performed in the wavelet domain (Li & Oldenburg 2003). In particular, by thresholding small wavelet coefficients and saving a sparse kernel matrix, memory and computational cost can be reduced significantly. The kernel matrix and model vector are transformed to the wavelet domain and multiplication makes predictions in the data domain. The efficiency gain of the wavelet compression depends on the level of wavelet transformation (sparseness) and thresholding value. The compression is applied row-wise to the kernel matrix. Hence, each row represents an approximation of the original kernel matrix. We considered various wavelets, levels, and threshold values and empirically chose the Daubechies-4 wavelet, level 2, and threshold values of 0.001 for the gravity kernel and 0.7 for the magnetic kernel. These settings significantly speed up the matrix multiplication in the 3-D forward model by $\sim 50 \times$ while the compression causes relative errors of 1.5 per cent. In Fig. 2, data prediction by the wavelet compression is compared with true data generated from a random 3-D model.

The proposal distribution applies the prior distribution when jumping between values for k to improve acceptance rates in *add* and *delete* steps (Dosso *et al.* 2014). In this work, Parallel Tempering (PT, Geyer 1991; Dettmer & Dosso 2012; Sambridge 2014) utilizes N_{PT} independent Markov chains for different values of temperature and allows for the exchange of model parameters between chains. This technique relaxes the likelihood function for large temperatures, increases the acceptance rate for model jumps, and avoids trapping into local modes. The PT is implemented via a master–worker structure with the message passing interface (MPI) to parallelize the inversion. Each PT chain is run on an individual processor resulting in N_{PT} workers.

3 RESULTS FOR SIMULATED DATA

This 3-D simulation includes a basement and two salt bodies embedded in sedimentary rocks. The basement consists of two layers with density contrasts of 0.35 and 0.25 g cm⁻³. The two salt bodies include a pyramid and a cuboid with density contrasts of -0.25 and -0.35 g cm⁻³,

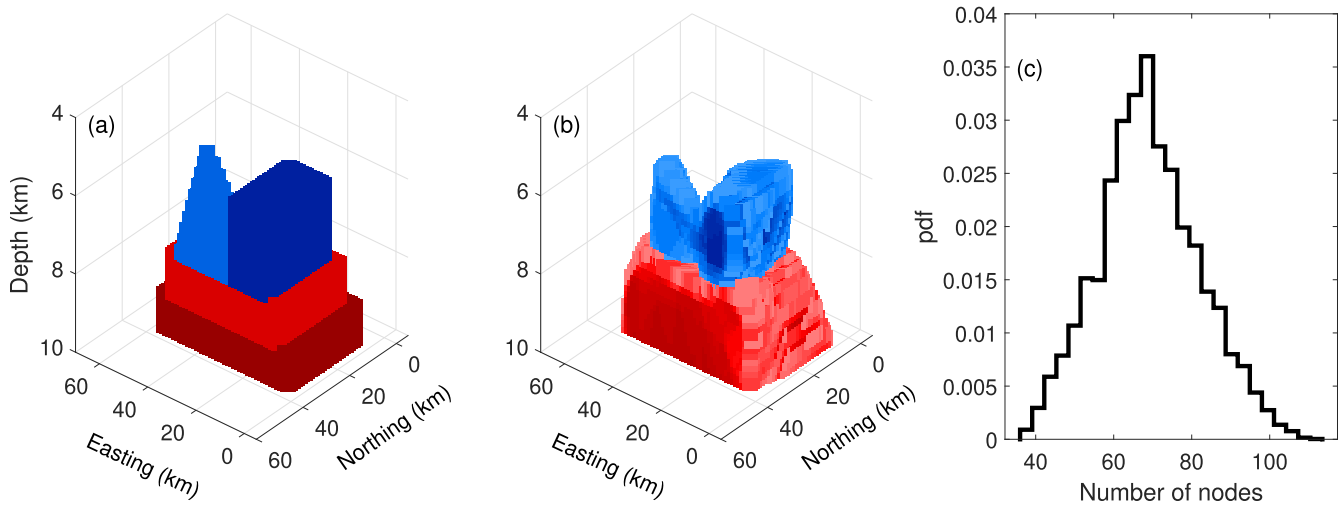


Figure 3. (a) True and (b) PM models. (c) Marginal distribution of the number of Voronoi nodes.

respectively. Other regions are assumed to be sedimentary rocks with no density contrast (Fig. 3a). The depths to the top of the pyramidal and cuboidal salts are 5 and 6 km, respectively. The basement relief has a depth of 8 km. The regular discretization for the forward model is by 64 prisms in the x , y and z directions (262 144 prisms). The size of each prism is 1000 by 1000 by 156 m. The density contrast priors for salt and basement are uniform over $(-0.4, -0.2)$ g cm $^{-3}$ and $(0.2, 0.4)$ g cm $^{-3}$, respectively. We assume zero susceptibility for sedimentary rocks and salt bodies. The prior for the number of nodes (k) in the spatial discretization is uniform between 6 and 120.

Correlated Gaussian noise with a standard deviation of 4 per cent of the maximum of the true gravity data is added to the true gravity data. The noise is correlated with $\text{AR}_x = [0.6, -0.5]$, $\text{AR}_y = 0.4$ and $\text{AR}_{xy} = -0.2$. To examine the ability of the algorithm to resolve uncorrelated residuals, we assume that the noise on the magnetic data is uncorrelated Gaussian distributed with a standard deviation of 6 per cent of the maximum of the true magnetic data. The prior pdfs for the AR coefficients are assumed to be bounded uniform and meet the stationary condition (Ghale noe 2022). Bounds for the first order are $(-0.85, 0.9)$, for the second order $(-0.85, 0.1)$, and for the third order $(-0.25, 0.25)$. The prior for the AR order is uniform between 0 and 3. Empirically, AR parameters converge faster than spatial parameters. Hence, we sample the noise model at 10 per cent of the MCMC steps. To improve *burn-in*, we assumed an AR(0) model during the first 5 per cent of MHG steps. This avoids that AR parameters initially fit major data features and leads to faster convergence.

The inversion is started from a model whose parameters are randomly derived from the prior. We applied PT with 40 parallel chains including 20 chains with a temperature of 1, and a temperature ratio of 1.2 for the remaining chains. During the initial *burn-in* phase, samples are not retained. During *sampling*, an ensemble of models is recorded for posterior inference. For interpretation, we consider the results in terms of averages of all recorded models (posterior mean – PM – model), various marginal distributions, and widths of 95 per cent credibility intervals (CIs).

Our method requires assigning rock types to 27 subspaces. Here, we assign the central space as salt body, the bottom-centre subspace as basement rocks, and the remaining 25 subspaces are assigned as sedimentary rocks. The inversion recorded 400 000 models.

Fig. 3 shows the PM model for density contrast which represents the true model well with the pyramid and cuboid salt bodies clearly resolved. In addition, the basement is imaged with a similar horizontal extent and at a similar depth as the true model. Finally, the marginal distribution for the number of nodes (Fig. 3c) peaks at 65 with uncertainty from 40 to 110. Therefore, the number of spatial parameters used in this inversion ranges from ~ 160 and ~ 400 , a significant dimension reduction over the underlying regular grid. This reduction is a key advantage of trans-D models.

Fig. 4 represents 2-D northing and easting slices of the 3-D results for the true and PM models, 95 per cent CI widths and the maximum *a posteriori* (MAP) model. These slices illustrate that the two different salt geometries are both resolved by the trans-D VP parametrization. The PM slices show that the interior density contrast of the cuboid salt body is lower than that of the pyramidoid which agrees with the true model. The widths of 95 per cent CIs are used to interpret the PM model uncertainty. Higher widths represent regions with higher uncertainty. Large widths may arise from metastable posterior distributions (Yao *et al.* 2020), such as multimodal or wide posterior distributions. In these regions, the PM model may not be representative of the posterior density, and care should be taken to avoid overinterpretation. For example, higher uncertainties can be found at the boundaries of structures. For example, at the top of the basement, rock salt (negative density contrasts) and basement (positive density contrasts) for various samples in the MCMC output ensemble may overlap. Therefore, the PM shows values around zero, but the posterior may be broad or even multimodal with modes of negative and positive density contrast. The MAP models are taken to be the maximum likelihood models for the peak of the k -distribution and indicate a close representation of the true model, although with sharp Voronoi polygons. These polygon shapes disappear in the PM model due to the ensemble averaging. Fig. 5 shows the noisy simulated data, the mean of the posterior predictive distribution, and 1-D slices through the 2-D data. Both gravity and magnetic predictions

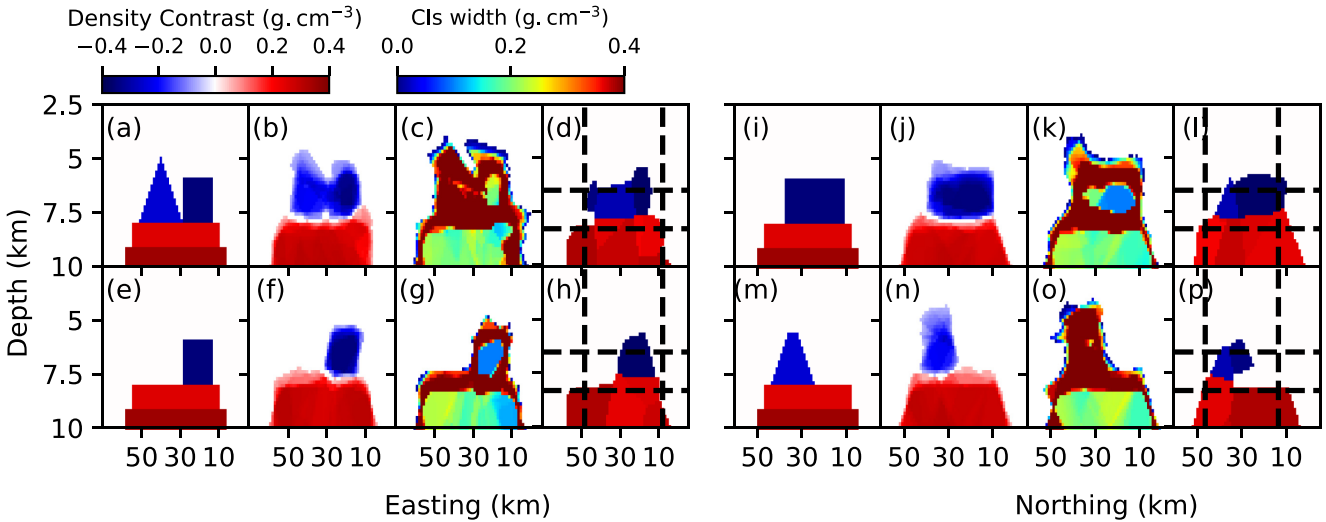


Figure 4. Slices at 40-km northing of (a) true, (b) PM, (c) 95 per cent CIs widths and (d) MAP model with locations of planes (dashed lines). (e–h) Same information for slice at 18-km northing. (i–l) Same information for slice at 24-km easting. (m–p) Same information for slice at 43-km easting.

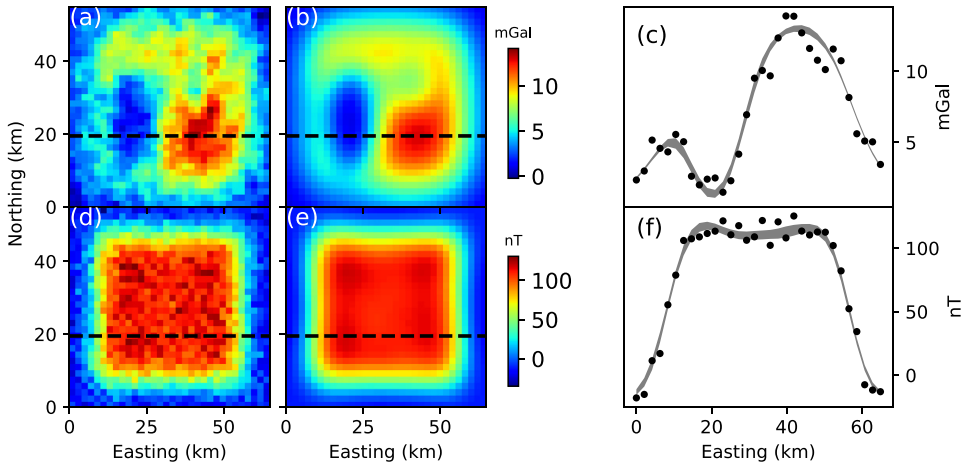


Figure 5. (a) Simulated noisy gravity anomaly, (b) PM of predicted gravity data, (c) slice through the 20-km northing (dashed line) of gravity data map showing simulated gravity data (black dots) and 95 per cent CIs width of predicted gravity data (grey lines). (d–f) The same information for the magnetic anomaly.

fit the data closely. Note that residual correlations are visible for the gravity data. These correlations are accounted for by the trans-D AR model.

Fig. 6 summarizes the results for the noise model in terms of marginal distributions. The simulated gravity data contain correlated noise with true orders of 2, 1 and 1 for AR_x , AR_y and AR_{xy} , respectively. These true AR orders are correctly resolved by the trans-D model with only modest uncertainty. The marginal distributions for the 2-D AR coefficients (Fig. 6) are also resolved with modes near true values. For magnetic data, uncorrelated errors were assumed. In that case, the 2-D AR model infers zero-order for AR_x and AR_y (Figs 6g–i) and order 1 for AR_{xy} . The marginal distributions for coefficients show peaks near zero (Figs 6j–l) in all cases. Therefore, even where the trans-D model permits higher AR orders, the predictions are nearly uncorrelated.

In order to examine how the trans-D AR model improves inversion results, the autocorrelation of raw and standardized residuals is shown (Fig. 7). We can see that gravity raw residuals exhibit significant correlation (Fig. 7a). The application of the trans-D AR model in 2-D successfully reduces correlation in standardized residuals (Fig. 7b). For magnetic data, raw and standardized residuals are uncorrelated (Figs 7e and f). Finally, histograms for standardized residuals closely match the standard normal distributions (Figs 7d and h). In summary, the trans-D AR model for 2-D data successfully quantifies the noise process and ensures that assumptions about noise are met in the inversion. This instills confidence that estimated parameter values and uncertainties are appropriate.

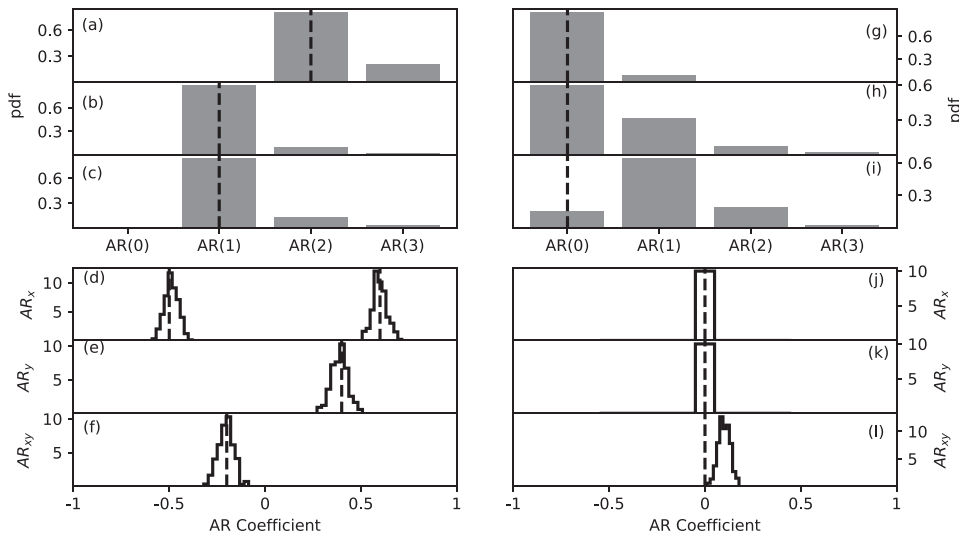


Figure 6. Marginal probability distributions of gravity AR model orders for (a) AR_x , (b) AR_y and (c) AR_{xy} , and (d–f) marginal probability distributions the corresponding coefficients at mode of the AR order marginals. True AR orders and coefficients are also shown (dashed lines). (g–l) The same information for magnetic AR models.

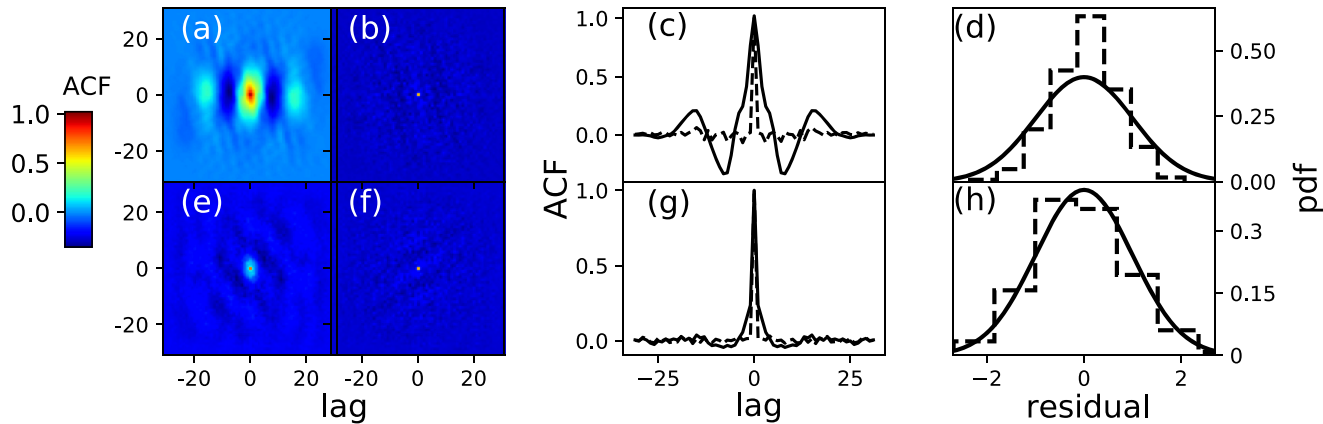


Figure 7. Spatial autocorrelation of (a) raw and (b) standardized residuals for gravity. (c) The middle row of maps in (a) and (b) with solid and dashed lines, respectively. (d) Histograms of standardized gravity residuals (dashed line), and the standard normal distribution (solid line). (e–h) The same information for magnetic residuals.

4 FIELD DATA IN 3-D APPLICATION

This section presents results for the application of the 3-D trans-D inversion to aerogravity and aeromagnetic data over the Ghasha oilfield offshore Abu Dhabi, UAE. The study area includes complex salt diapirs and basement topography which makes it an ideal study site for the proposed method. Results are interpreted in terms of Earth structures and noise models.

The gravity and magnetic data were acquired by Sander Geophysics Ltd. (SGL) for ADNOC in 2007–2008 (Ali *et al.* 2017). Data corrections were applied in terms of Eötvös, latitude, free air, Bouguer, the curvature of the Earth, terrain, static and levelling corrections. The terrain correction uses a density of 2.6 g cm^{-3} for land and terrain-topographic data obtained by the Shuttle Radar Topography Mission (SRTM). The seawater-depth correction uses a density of 1.02 g cm^{-3} over marine areas from bathymetric data provided by the Gridded Bathymetric Chart of the Oceans 1-min grid. Regional effects were computed and removed by applying a low-pass filter with a 3-km half-wavelength and upward continued to 20 km above sea level. Ultimately, data were gridded at 1 km by 1 km.

The aeromagnetic survey applied Caesium optically pumped magnetometers with a 0.001 nano Tesla (nT) sensitivity and sensor noise of 0.02 nT. Data corrections included removal of the International Geomagnetic Reference Field (IGRF), leveling error corrections, and diurnal fluctuation corrections. Ultimately, differentially-reduced-to-the-pole (DRTP) data were calculated (Salem & Ali 2016) and provided to us and are used for the inversion.

We studied a region of 65-km-EW extent, and 50-km-NS extent, including the Ghasha oilfield and diapiric island of Sir Bani Yas (Fig. 8). The area is sampled by a grid of 32 by 32 points for gravity and magnetic data. The model space spans dimensions of $75 \text{ km} \times 60 \text{ km} \times 10 \text{ km}$. The regular grid for forward computations has 64 by 64 by 64 regular prisms. The model space is extended by 5 km beyond the data

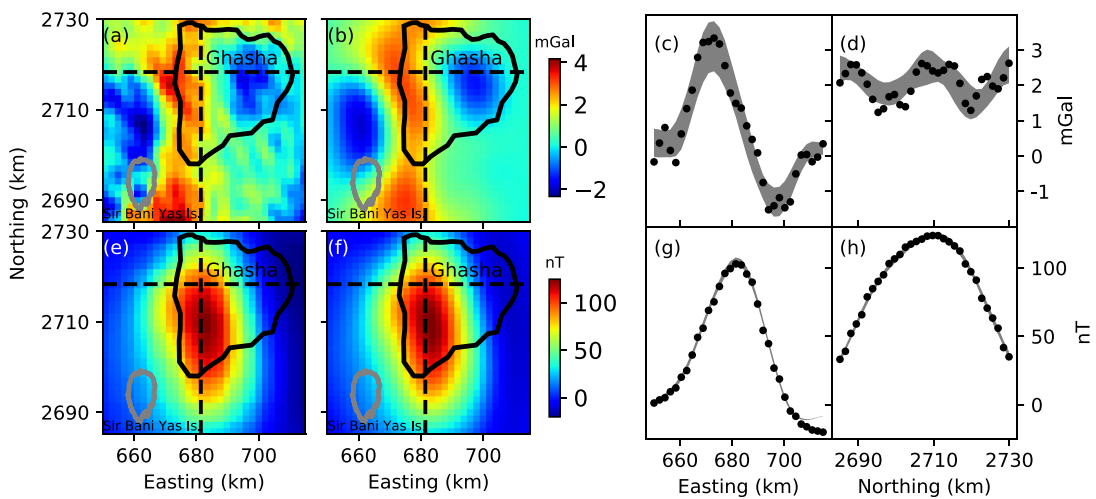


Figure 8. (a) Gravity anomaly, (b) PM of predicted gravity data, (c) slice through 2718-km northing of the gravity anomaly map showing observed gravity anomaly (black dots) and 95 per cent CI widths from predicted gravity data (grey area), (d) slice through 682-km easting. The Location of both slices is indicated in (a) and (b) by dashed lines. (e–h) The same information for the magnetic anomaly. Coastlines (grey) and outlines of the Ghasha oilfield (solid black) are also shown in (a, b, e and f). The map coordinates are in UTM Zone 39 N, WGS84.

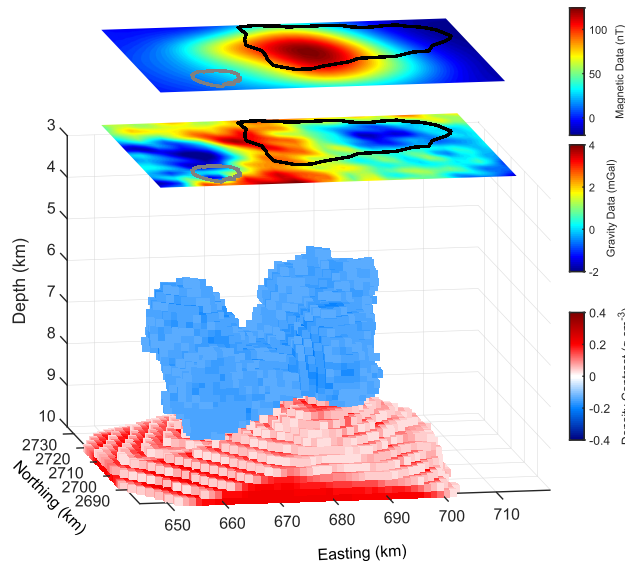


Figure 9. 3-D PM model for density contrast (bottom), and a projection of the observed gravity (middle) and magnetic (top) anomalies at the Earth's surface. The basement is represented with positive density contrast (red colours), and two salt diapirs are imaged with negative density contrast (blue colours). The background white colour shows sedimentary rocks.

sampling on all sides in the horizontal direction to reduce the effects from subsurface structures beyond the data region. The depth range of the model space is from 0 to 10 km. The field-data inversion is carried out with the same prior pdfs and assumptions as were applied for simulated data, except for the prior pdf for salt body which is uniform over $(-0.5, -0.2)$ g cm $^{-3}$. In addition, the prior for z parameter is uniform over (4.5, 10) km. The MHG sampling with PT was based on 40 chains computed in parallel via MPI. The posterior sample includes 800 000 models and the total run time was 5 days.

Fig. 8 shows observed and predicted data with the good agreement throughout the survey area. For more detailed consideration, EW slices at 2718-km northing and NS slices at 682-km easting are also shown (Figs 8c and d). The slices illustrate that the predicted data capture the main features of the field data. In addition, the width of the 95 per cent CI of the posterior predictive distribution matches smaller fluctuations in the data. However, some smaller features are not captured by our model. For example, the location of Sir Bani Yas Island shows a negative gravity anomaly with a spatial extent of about 8 pixels. This feature is not captured in the data prediction.

Fig. 9 is a 3-D image of the PM model for density contrast and shows a projection of the gravity and magnetic data at the Earth's surface. In this image, only rock salts with density contrast lower than -0.13 g cm $^{-3}$ are shown. This aims to better visualize the salt boundary with sedimentary rocks. The value of -0.13 g cm $^{-3}$ is based on the Infracambrian Hormuz salt outcrops in the Jabal Dhanna peninsula and on Sir Bani Yas Island (Geng *et al.* 2020). Interestingly, the 3-D model shows dome shapes for both salt diapirs. The locations of two salt diapirs

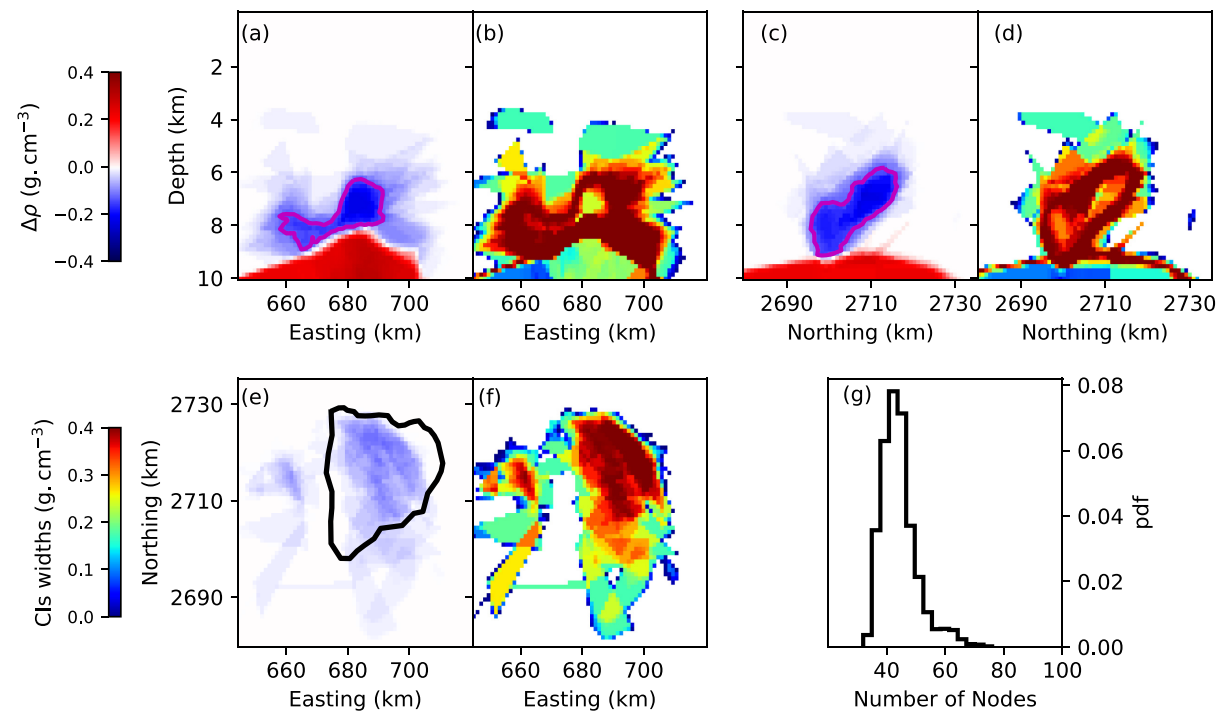


Figure 10. Slices through the PM model and 95 per cent CI widths at 2700-km northing, 662-km easting and 5.4-km depth in (a–b), (c–d) and (e–f), respectively. The density contrast of -0.13 g cm^{-3} (magenta line) and the boundary of Ghasha oilfield (black line) are outlined. (g) Marginal probability distribution of k .

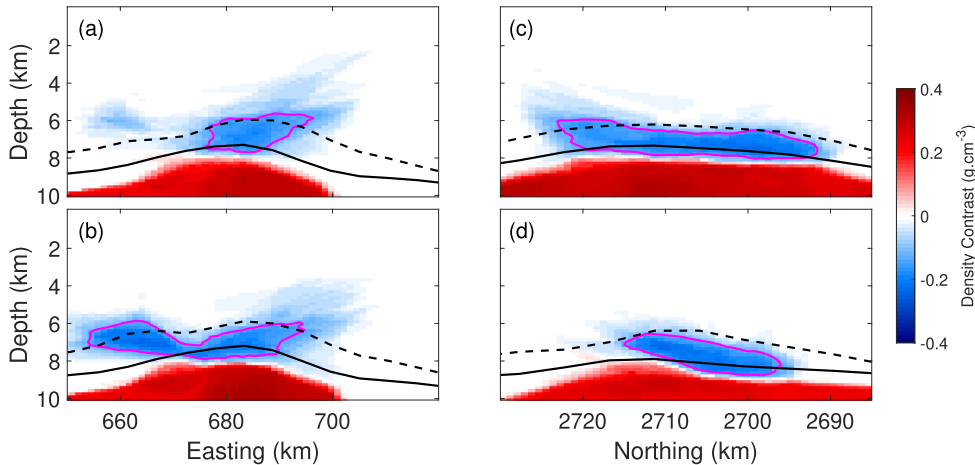


Figure 11. Comparison of our results to results from linearized, regularized inversion (Kabirzadeh et al. 2021). Slices are shown through the PM model at (a) 2717.5-km northing, (b) 2711.4-km northing, (c) 679.5-km easting and (d) 668.8-km easting. Depths to the basement (solid black line) and salt (dashed black line) from Kabirzadeh et al. (2021) are also shown. The extent of the salt body in the PM model is interpreted to be the boundary of a density contrast of -0.13 g cm^{-3} (magenta line).

do not exactly align with the locations of two negative peaks in the observed gravity anomaly. This is due to the joint inversion resolving the rock salt in the presence of basement topography. Resolving the basement topography is aided by the information content from magnetic data. The basement underlying the salt is undulating, and its minimum depth reaches around 8.5 km.

Fig. 10 shows posterior results in terms of 2-D slices through the 3-D volume. The PM models, the width of 95 per cent CIs, and the marginal for the number of nodes are shown. The slice at 2700-km northing shows two salt structures (magenta line -0.13 g cm^{-3}) with the shallower at around 6-km depth. At this slice, the salt body is imaged with no high negative peak in gravity data because the negative anomaly is compensated with relatively large positive density from the basement topography which can be estimated from the large positive magnetic anomaly at this area. The slice at 662-km easting indicates a salt body with high negative density contrasts and is consistent with the high negative gravity anomaly (from 2700-km to 2720-km northing). Interestingly, the extent of salt in the horizontal slice of the PM model at the depth of 5.4 km approximately matches the boundary of the Ghasha oilfield (Fig. 10e). The maps of the widths of 95 per cent CIs show the largest uncertainty close to the boundary between basement rocks and rock salt due to overlapping of both positive and negative density

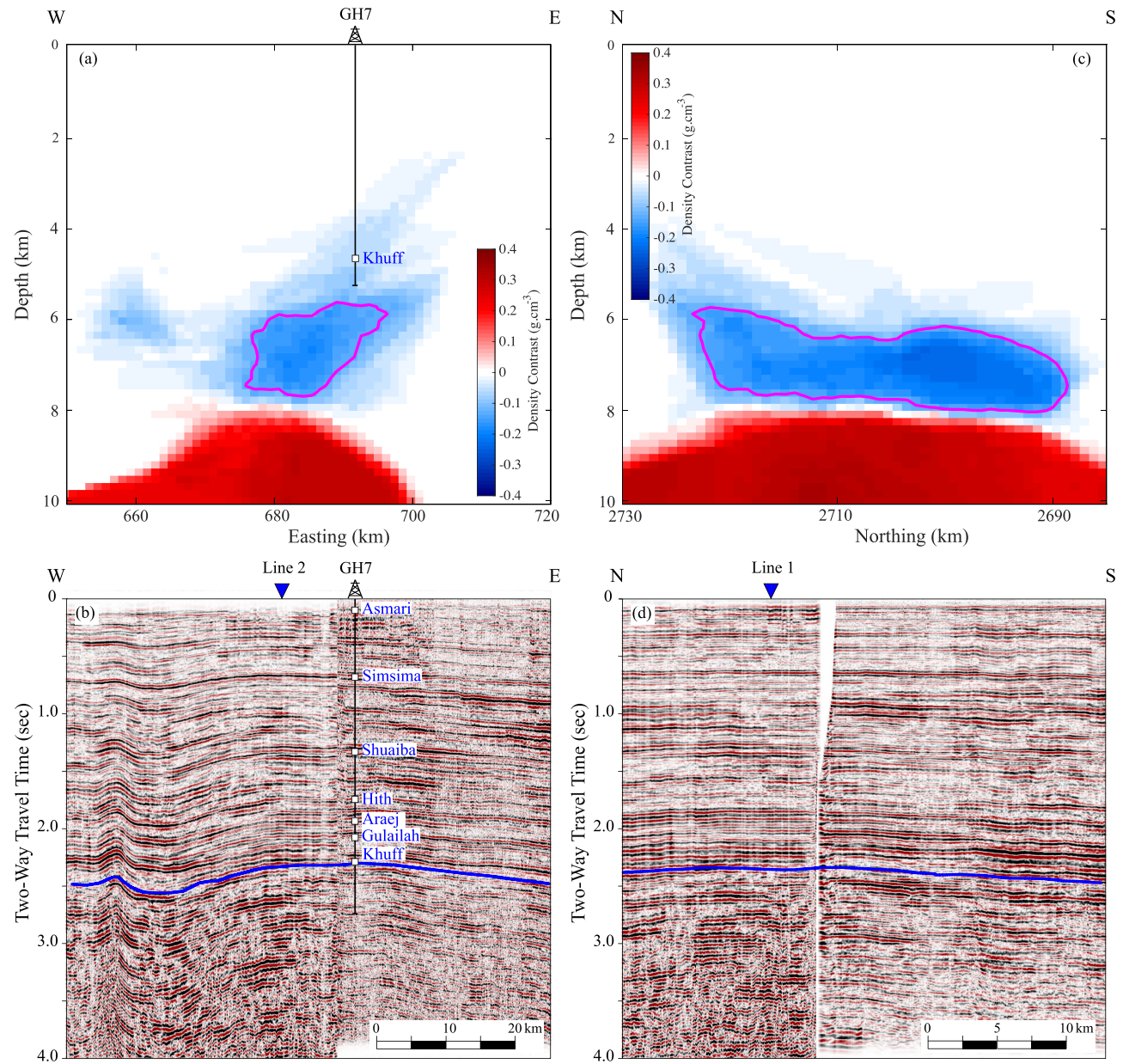


Figure 12. (a) PM density contrast model along with seismic profile 1 at 2718-km northing. (b) Seismic profile 1, which crosses borehole GH7. (c) PM model showing inverted density along with seismic profile 2 at 682-km easting. (d) Seismic profile 2. The magenta line on the density contrast model corresponds to a density contrast of -0.13 g cm^{-3} , which is interpreted as the top of the salt body. The blue lines on the seismic profiles depict the top Khuff Formation, the deepest formation penetrated by the GH7 well. The inverted triangles on the seismic profiles show seismic lines that cross this profile. For the location of the profiles, see Fig. 8.

contrast at the same space in the ensemble of posterior models. The marginal probability distribution of the number of nodes peaks at 45 nodes with uncertainty from 30 to 80 nodes (Fig. 10g).

In Fig. 11, our results are compared to the previous work based on Levenberg–Marquardt inversion that assumes known density contrasts and is linearized (Kabirzadeh *et al.* 2021). Fig. 11 shows the estimated boundaries of basement and salt for two EW and two NS slices. Our results are shown in terms of the PM model. Generally, both methods resolve similar structures, but important differences exist. The linearized inversion produces globally smooth models and spatial resolution does not adapt locally based on data information. In contrast, our results adapt model complexity based on data information. For example, our results infer that the two salt structures are nearly separated at 675 km easting (Fig. 11b). At the same location, the regularized inversion suggests a more continuous salt body.

Fig. 12 considers seismic profiles that cross the Ghasha field and our inversion results. Locations of the profiles are shown in Fig. 8. Note that the Ghasha salt has not been successfully imaged by seismic data to date, due to the thick sediment cover. In addition, wells have not sampled the salt body (e.g. well GH7, see Fig. 12). Nonetheless, comparison with gravity results provides useful insights. We infer the

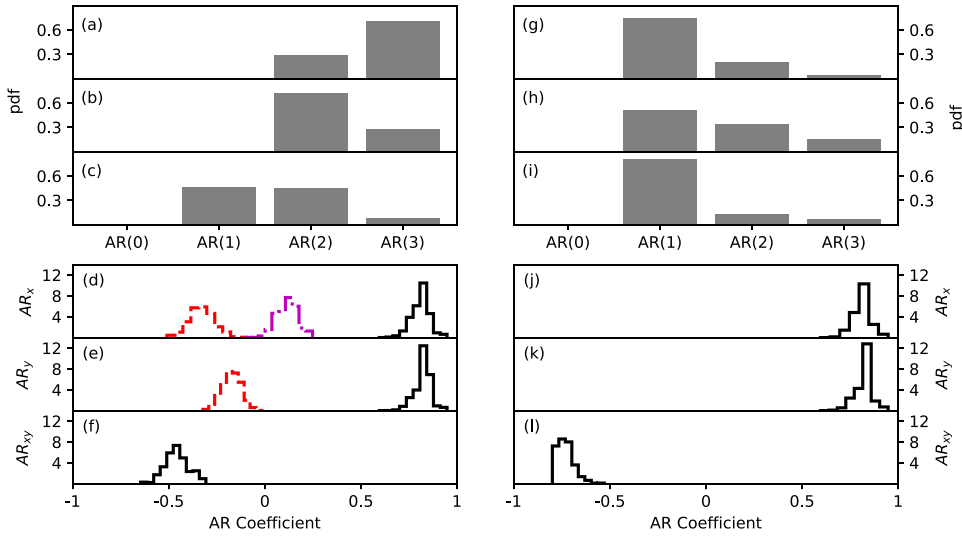


Figure 13. The marginal probability distributions of gravity AR model order for (a) \mathbf{AR}_x , (b) \mathbf{AR}_y and (c) \mathbf{AR}_{xy} . The marginal probability distributions of sampled gravity AR coefficients for (d) \mathbf{AR}_x , (e) \mathbf{AR}_y and (f) \mathbf{AR}_{xy} . The black, red and magenta distributions are for the first, the second and the third AR coefficient, respectively. (g–l) The same information but for magnetic AR model.

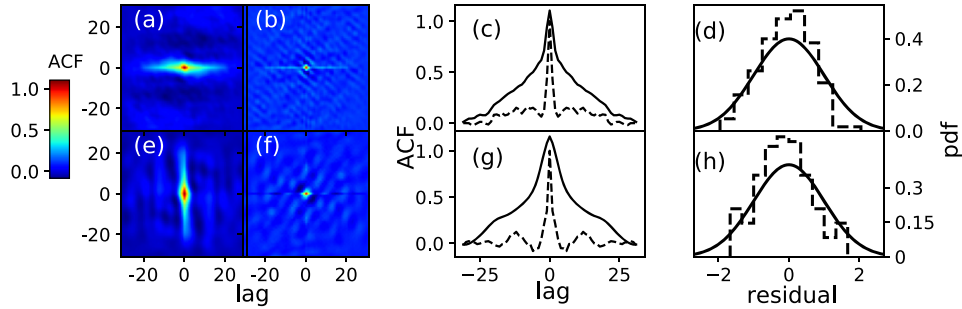


Figure 14. Autocorrelation of (a) gravity raw residuals, (b) gravity standardized residuals. (c) A slice through the middle row in map (a) is shown (solid line) and a slice of map (b) is shown (dashed line). (d) Histogram of standardized gravity residuals (dashed line) and the standard normal distribution (solid line). (e–h) The same information for magnetic residuals.

salt to occur between the Khuff Formation and the basement, at a depth not reached by the well or imaged by the seismic data. In addition, the shape of the Khuff formation imaged by the seismic data resembles that of the shape we infer for the salt body.

The results for the trans-D AR model for 2-D data are shown in Fig. 13. Gravity residuals are strongly correlated with modes at third, second and first order for \mathbf{AR}_x , \mathbf{AR}_y and \mathbf{AR}_{xy} , respectively. Magnetic residuals show correlation at the first order in all three directions. The marginal distributions of the AR coefficients imply the first coefficient is at values near 0.9 while the other coefficients are significantly lower. This means that correlations exhibit exponential decay.

Fig. 14 shows the autocorrelation of raw and standardized residuals to investigate the performance of the spatial trans-D AR model. The results show (Figs 14a, b, e and f) that our method successfully reduces the correlation of residuals for gravity and the magnetic data. The exponential decay mentioned previously is clear when considering the autocovariance function of the residuals (Figs 14c and g). Finally, the Gaussianity of standardized residuals agrees well with the standard normal distribution. Therefore, the trans-D AR model for 2-D spatial data significantly improves noise treatment in this study.

5 DISCUSSION AND CONCLUSION

In joint gravity and magnetic inversion, a more complex model of the Earth's subsurface requires a parametrization with a higher spatial resolution. In addition, data spatial resolution varies throughout the model space and a parametrization should locally adapt to the resolving power of the data. Trans-D models provide variable spatial resolution based on data information without requiring regularization.

For the inversion of gravity and magnetic anomalies, we used hierarchical partitioning of 3-D space based on Voronoi nodes and six planes to parametrize the spatial Earth model. The simulated and field data inversions produced solutions with significant basement topography, multiple salt diapirs and excellent data fit. These results were achieved with small numbers of Voronoi nodes (peaking at 45 nodes) for the

field data. Therefore, the parametrization is parsimonious with far fewer parameters than required for regular grids. As a result, numerical integration via MHG sampling is possible.

Addressing error correlations in potential field data measured at the Earth's surface is more complex than similar approaches in 1-D data (time series or spatial transects). We introduced a trans-D AR noise model for 2-D data to estimate correlations in two horizontal and one diagonal directions. We showed that this trans-D AR noise model can account for complex noise correlations with up to three AR coefficients in each of the three directions. *A posteriori* residual analysis was applied to show that the trans-D AR model dramatically reduced the correlations in residuals. Therefore, the density estimates account for noise correlations.

The hierarchical partitioning we applied worked well for imaging locations with individual salt diapirs in the presence of basement topography. However, other applications may require additional work. For example, modifications may be required to resolve multiple salt diapirs that are significantly separated in space and/or exhibit more complex boundaries. In addition, a clear limitation of the method is the requirement to assign rock types to the 27 subspaces created by the six planes. Other hierarchical models are possible to reduce ambiguity in this process. For example, the combination of linear interpolation and alpha shapes (Ghalenoei 2022) was successfully applied to a 2-D problem. However, the method is associated with higher computational cost. Alternatively, nested Voronoi partitioning (Ghalenoei *et al.* 2021) may also be applied in 3-D applications, which could be beneficial for 3-D inversions where many diapir structures are present.

In conclusion, our study demonstrated that data-driven estimation of 3-D density and susceptibility distributions in the Earth's subsurface is improved by incorporating prior knowledge in the spatial parametrization and by carefully parametrizing the typically highly correlated noise on data.

ACKNOWLEDGMENTS

We thank Dr Richard Holme and an anonymous reviewer for their helpful comments that improved the quality of the paper. Elements of this study were supported by the Khalifa University of Science, Technology and Research under Award No. CIRA-2019-008. We wish to thank ADNOC for permission to use the data in this study.

DATA AVAILABILITY

The inversion Python code and simulated data for this paper are available on GitHub, at https://github.com/emadghalenoei/3D_Voronoi_Plane_Trans-D_Inversion. Field data will be shared upon request to the corresponding author and after permission from ADNOC.

REFERENCES

- Aitken, A., Salmon, M. & Kennett, B., 2013. Australia's Moho: a test of the usefulness of gravity modelling for the determination of Moho depth, *Tectonophysics*, **609**, 468–479.
- Ali, M., Fairhead, J., Green, C. & Noufal, A., 2017. Basement structure of the United Arab Emirates derived from an analysis of regional gravity and aeromagnetic database, *Tectonophysics*, **712**, 503–522.
- Altman, N.S., 1992. An introduction to kernel and nearest-neighbor non-parametric regression, *Am. Stat.*, **46**(3), 175–185.
- Blakely, R.J., 1996. *Potential Theory in Gravity and Magnetic Applications*, Cambridge Univ. Press.
- Bodin, T. & Sambridge, M., 2009. Seismic tomography with the reversible jump algorithm, *Geophys. J. Int.*, **178**(3), 1411–1436.
- Bodin, T., Sambridge, M. & Gallagher, K., 2009. A self-parametrizing partition model approach to tomographic inverse problems, *Inverse Problems*, **25**(5), 055009, doi:10.1088/0266-5611/25/5/055009.
- Boulanger, O. & Chouteau, M., 2001. Constraints in 3d gravity inversion, *Geophys. Prospect.*, **49**(2), 265–280.
- Camacho, A.G., Montesinos, F.G. & Vieira, R., 2000. Gravity inversion by means of growing bodies, *Geophysics*, **65**(1), 95–101.
- Chen, L. & Liu, L., 2019. Fast and accurate forward modelling of gravity field using prismatic grids, *Geophys. J. Int.*, **216**(2), 1062–1071.
- Dettmer, J. & Dosso, S.E., 2012. Trans-dimensional matched-field geoaoustic inversion with hierarchical error models and interacting markov chains, *J. acoust. Soc. Am.*, **132**(4), 2239–2250.
- Dettmer, J., Dosso, S.E. & Holland, C.W., 2007. Uncertainty estimation in seismo-acoustic reflection travel time inversion, *J. acoust. Soc. Am.*, **122**(1), 161–176.
- Dettmer, J., Molnar, S., Steininger, G., Dosso, S.E. & Cassidy, J.F., 2012. Trans-dimensional inversion of microtremor array dispersion data with hierarchical autoregressive error models, *Geophys. J. Int.*, **188**(2), 719–734.
- Dosso, S.E., Dettmer, J., Steininger, G. & Holland, C.W., 2014. Efficient trans-dimensional Bayesian inversion for geoaoustic profile estimation, *Inverse Problems*, **30**(11), 114018.
- Fix, E. & Hodges, J.L., 1989. Discriminatory analysis. nonparametric discrimination: consistency properties, *Int. Stat. Rev./Revue Internationale de Statistique*, **57**(3), 238–247.
- Geng, M., Ali, M.Y., Fairhead, J.D., Bouzidi, Y. & Barkat, B., 2020. Morphology of the basement and Hormuz salt distribution in offshore Abu Dhabi from constrained 3-D inversion of gravity and magnetic data, *Tectonophysics*, **791**, 228563, doi:10.1016/j.tecto.2020.228563.
- Geyer, C.J., 1991. Markov Chain Monte Carlo maximum likelihood, Interface Foundation of North America. Retrieved from the University of Minnesota Digital Conservancy, <https://hdl.handle.net/11299/58440>.
- Ghalenoei, E., 2022. Probabilistic joint inversion of gravity and magnetic data with 3D trans-dimensional earth and noise models, *Unpublished doctoral thesis*, University of Calgary, Calgary, AB.
- Ghalenoei, E., Dettmer, J., Ali, M.Y. & Kim, J.W., 2021. Gravity and magnetic joint inversion for basement and salt structures with the reversible-jump algorithm, *Geophys. J. Int.*, **227**(2), 746–758.
- Green, P.J., 1995. Reversible jump Markov Chain Monte Carlo computation and Bayesian model determination, *Biometrika*, **82**(4), 711–732.
- Hawkins, R. & Sambridge, M., 2015. Geophysical imaging using trans-dimensional trees, *Geophys. J. Int.*, **203**(2), 972–1000.
- Hinze, W.J., Von Frese, R.R., Von Frese, R. & Saad, A.H., 2013. *Gravity and Magnetic Exploration: Principles, Practices, and Applications*, Cambridge Univ. Press.
- Izquierdo, K., Lekić, V. & Montési, L.G., 2020. A Bayesian approach to infer interior mass anomalies from the gravity data of celestial bodies, *Geophys. J. Int.*, **220**(3), 1687–1699.
- Johnson, J., Douze, M. & Jégou, H., 2019. Billion-scale similarity search with GPUS, *IEEE Trans. Big Data*, **7**(3), 535–547.

- Jorgensen, G.J. & Kisabeth, J.L., 2000. Joint 3-D inversion of gravity, magnetic and tensor gravity fields for imaging salt formations in the deepwater Gulf Of Mexico, in *SEG Technical Program Expanded Abstracts 2000*, pp. 424–426, Society of Exploration Geophysicists.
- Kabirzadeh, H., Ali, M.Y., Lee, G.H. & Kim, J.W., 2021. Determining infracambrian Hormuz salt and basement structures offshore Abu Dhabi by joint analysis of gravity and magnetic anomalies, *SPE Reserv. Eval. Eng.*, **24**(01), 238–249.
- Kamm, J., Lundin, I.A., Bastani, M., Sadeghi, M. & Pedersen, L.B., 2015. Joint inversion of gravity, magnetic, and petrophysical data—a case study from a Gabbro intrusion in Boden, Sweden, *Geophysics*, **80**(5), B131–B152.
- Kolb, J. & Lekić, V., 2014. Receiver function deconvolution using transdimensional hierarchical Bayesian inference, *Geophys. J. Int.*, **197**(3), 1719–1735.
- Krahenbuhl, R.A. & Li, Y., 2009. Hybrid optimization for lithologic inversion and time-lapse monitoring using a binary formulation, *Geophysics*, **74**(6), 155–165.
- Lelievre, P.G. & Farquharson, C.G., 2013. Gradient and smoothness regularization operators for geophysical inversion on unstructured meshes, *Geophys. J. Int.*, **195**(1), 330–341.
- Lelièvre, P.G., Barnoud, A., Niess, V., Carloganu, C., Cayol, V. & Farquharson, C.G., 2019. Joint inversion methods with relative density offset correction for muon tomography and gravity data, with application to volcano imaging, *Geophys. J. Int.*, **218**(3), 1685–1701.
- Li, Y. & Oldenburg, D.W., 1996. 3-D inversion of magnetic data, *Geophysics*, **61**(2), 394–408.
- Li, Y. & Oldenburg, D.W., 1998. 3-D inversion of gravity data, *Geophysics*, **63**(1), 109–119.
- Li, Y. & Oldenburg, D.W., 2003. Fast inversion of large-scale magnetic data using wavelet transforms and a logarithmic barrier method, *Geophys. J. Int.*, **152**(2), 251–265.
- Luo, X., 2010. Constraining the shape of a gravity anomalous body using reversible jump Markov Chain Monte Carlo, *Geophys. J. Int.*, **180**(3), 1067–1079.
- Maag, E. & Li, Y., 2018. Discrete-valued gravity inversion using the guided fuzzy C-means clustering technique, *Geophysics*, **83**(4), G59–G77.
- MacKay, D.J., et al., 2003. *Information Theory, Inference and Learning Algorithms*, Cambridge Univ. Press.
- Malinverno, A. & Leaney, S., 2000. A monte carlo method to quantify uncertainty in the inversion of zero-offset Vsp data, in *SEG Technical Program Expanded Abstracts 2000*, pp. 2393–2396, Society of Exploration Geophysicists.
- Martinez, C., Li, Y., Krahenbuhl, R. & Braga, M., 2010. 3d inversion of airborne gravity gradiometry for iron ore exploration in Brazil, in *SEG Technical Program Expanded Abstracts 2010*, pp. 1753–1757, Society of Exploration Geophysicists.
- Martinez, C., Li, Y., Krahenbuhl, R. & Braga, M.A., 2013. 3D inversion of airborne gravity gradiometry data in mineral exploration: a case study in the Quadrilátero Ferrífero, Brazil, *Geophysics*, **78**(1), B1–B11.
- Michelini, A., 1995. An adaptive-grid formalism for traveltime tomography, *Geophys. J. Int.*, **121**(2), 489–510.
- Mojiri, A., Waghei, Y., Sani, H.N. & Borzadaran, G.M., 2018. The stationary regions for the parameter space of unilateral second-order spatial ar model, *Rand. Oper. Stochast. Eq.*, **26**(3), 185–191.
- Mosegaard, K. & Tarantola, A., 1995. Monte carlo sampling of solutions to inverse problems, *J. geophys. Res.*, **100**(B7), 12 431–12 447.
- Pallero, J., Fernández-Martínez, J.L., Bonvalot, S. & Fudym, O., 2017. 3D gravity inversion and uncertainty assessment of basement relief via particle swarm optimization, *J. Appl. Geophys.*, **139**, 338–350.
- Piana Agostinetti, N., Giacomuzzi, G. & Malinverno, A., 2015. Local three-dimensional earthquake tomography by trans-dimensional Monte Carlo sampling, *Geophys. J. Int.*, **201**(3), 1598–1617.
- Pilia, S., Jackson, J., Hawkins, R., Kaviani, A. & Ali, M., 2020. The southern Zagros collisional Orogen: new insights from transdimensional trees inversion of seismic noise, *Geophys. Res. Lett.*, **47**(4), e2019GL086258.
- Portniaguine, O. & Zhdanov, M.S., 2002. 3-d magnetic inversion with data compression and image focusing, *Geophysics*, **67**(5), 1532–1541.
- Ray, A., 2021. Bayesian inversion using nested trans-dimensional Gaussian processes, *Geophys. J. Int.*, **226**(1), 302–326.
- Salem, A. & Ali, M.Y., 2016. Mapping basement structures in the north-western offshore of Abu Dhabi from high-resolution aeromagnetic data, *Geophys. Prospect.*, **64**(3), 726–740.
- Sambridge, M., 2014. A parallel tempering algorithm for probabilistic sampling and multimodal optimization, *Geophys. J. Int.*, **196**(1), 357–374.
- Sambridge, M. & Mosegaard, K., 2002. Monte Carlo methods in geophysical inverse problems, *Rev. Geophys.*, **40**(3), 3–1.
- Sambridge, M., Braun, J. & McQueen, H., 1995. Geophysical parametrization and interpolation of irregular data using natural neighbours, *Geophys. J. Int.*, **122**(3), 837–857.
- Sambridge, M., Gallagher, K., Jackson, A. & Rickwood, P., 2006. Transdimensional inverse problems, model comparison and the evidence, *Geophys. J. Int.*, **167**(2), 528–542.
- Silva Dias, F.J., Barbosa, V.C. & Silva, J.B., 2011. Adaptive learning 3D gravity inversion for salt-body imaging, *Geophysics*, **76**(3), I49–I57.
- Stenerud, V.R., Lie, K.-A. & Kippe, V., 2009. Generalized travel-time inversion on unstructured grids, *J. Petrol. Sci. Eng.*, **65**(3–4), 175–187.
- Uieda, L. & Barbosa, V.C., 2012. Robust 3D gravity gradient inversion by planting anomalous densities, *Geophysics*, **77**(4), G55–G66.
- Uieda, L. & Barbosa, V.C., 2017. Fast nonlinear gravity inversion in spherical coordinates with application to the South American Moho, *Geophys. J. Int.*, **208**(1), 162–176.
- Wu, L., 2016. Efficient modelling of gravity effects due to topographic masses using the Gauss–FFT method, *Geophys. Suppl. Mon. Not. R. Astron. Soc.*, **205**(1), 160–178.
- Yao, Y., Vehtari, A. & Gelman, A., 2020. Stacking for non-mixing Bayesian computations: the curse and blessing of multimodal posteriors, preprint (arXiv:2006.12335).
- Zhou, H.-W., Li, L., Bjorklund, T. & Thornton, M., 2010. A comparative analysis of deformable layer tomography and cell tomography along the Larse lines in southern California, *Geophys. J. Int.*, **180**(3), 1200–1222.